



Research paper

## Analysis of a Linear Induction Motor with Solid Iron Secondary

S. E. Abdollahi<sup>1</sup>, M. Mirzaei<sup>2,\*</sup>

<sup>1</sup>Electrical and Computer Engineering Dept., Babol Noshirvani University of Technology, Babol, Iran.

<sup>2</sup>Electrical Engineering Dept., Amirkabir University of Technology, Tehran, Iran.

### Article Info

#### Article History:

Received 17 March 2017

Revised 29 July 2017

Accepted 11 November 2017

#### Keywords:

Iron secondary

Analytical calculations

Finite element method

Eddy currents

Linear induction motors

Thrust force

\*Corresponding Author's Email

Address: e.abdollahi@nit.ac.ir

### Extended Abstract

**Background and Objectives:** Linear induction motors (LIMs) are widely employed in rail transportation systems due to their robust, simple and low cost structure.

**Methods:** Several methods have evaluated various topologies' performances in the literature. These methods are more and less effective in the intended structures. In this paper, a new two-dimensional analytical method is presented in order to predict developed thrust force of a single-sided linear induction motor with a solid iron secondary.

**Results:** The skin and saturation effects of the induced eddy currents in the solid iron of the secondary are considered in the proposed method. The analytical results are then compared with the 2D finite element simulation and the experimental ones of the research work of Gieras et al. .

**Conclusion:** Results confirm the accuracy of the proposed analytical and finite element methods for the analysis and design of linear induction motors with solid iron secondary.

### Introduction

The linear motors are widely employed in various industrial applications including transportation [1] [2] [3] [4] [5], compressors [6], automation [7][8] and electromagnetic launch systems [9] [9] [10]. Linear Induction Motor (LIM) in its both double-sided and single-sided topologies is a suitable candidate for propulsion of train due to their simple structure [1][11]. An analysis of a double-sided LIM is presented in [4] that is employed for urban air-bus transit system.

But single-sided LIMs are more suitable for transportation because of their simpler structure [12] [13] [14]. In addition, due to the long secondary and short primary of single-sided LIMs, adjustment of air-gap is easier in transportation system. The primary winding of the Single Sided LIM (SSLIM) is composed of conventional distributed winding with half-

filled end slots (Fig. 1). SSLIMs, secondary could be double-layer with a solid back-iron layer and another thin aluminum sheet or just a single-layer with solid iron [15]. Also, implementation of single-layer solid iron secondary SSLIM is easier for transportation purposes than a double-layer secondary (Fig. 2). The magnetizing current of SSLIMs with solid-iron secondary is low due to the smaller magnetic air-gap. The thrust force versus speed curve of solid-iron secondary LIMs is close to a flat shape, which could provide a suitable acceleration thrust force [16] [17]. Employment of a suitable analysis method for the design and optimization of LIMs with solid-iron secondary is essential, especially for large ones employed in transportation applications. In this regard, the skin and saturation effects in solid-iron of secondary should be considered that significantly affect motor performance [18].

Numerical methods like finite difference or finite element are almost precise methods for analysis of

induced eddy currents in the solid irons but, they are time-consuming for design process of large linear induction motors [19][20][21]. Analytical methods by consideration of skin and saturation effects of solid iron secondary of SSLIM could be faster than the finite element analysis [15][22][21]. Several analytical methods were presented for eddy current analysis in the saturated solid iron for pulsating waves and traveling waves. The first analytical method modeled the iron saturation using a step-function method called limiting theory [23]. The results of limiting theory method for eddy current modeling in saturated solid iron were used for modeling solid-iron rotors or secondary of induction motors, which is related to traveling wave [17]. The limiting theory method was an approximate analytical method based on experimental results, which is not generally accurate enough. The other employed analytical method was a multilayer method for analysis of the induced eddy currents in saturated solid irons and steels [24]. Although the multilayer method could be used for pulsating waves and traveling waves, motor modeling presented by this method is not simple. It is also more complicated than the limiting theory method. The third method employed in saturated solid iron is based on modeling the B-H curve of solid iron using a parabolic function [25][26][27][28]. This method provides a complete solution of the induced eddy currents in saturated solid irons and steels. This method obtains the equivalent permeability of solid iron, and traveling waves in solid-rotor induction motors are directly calculated without consideration of air-gap [26]. The secondary loss and efficiency of a SSLIM is calculated in [28] based on 3D space harmonic method for composite secondary, whereas in the case of solid back iron, the saturation effect is not considered.

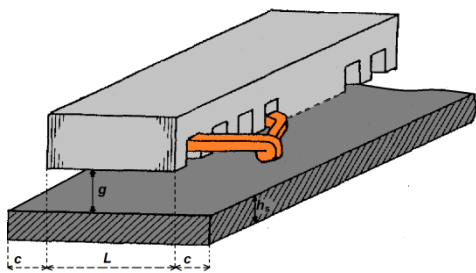


Fig. 1: Linear induction motor with solid iron secondary [6]

In this paper, parabolic function for the B-H curve of solid irons and steels is employed for analysis of traveling-wave eddy currents in the solid-iron secondary of SSLIM, in which air-gap is directly considered. The analytical calculations are compared with the experimental (obtained from [16]) and finite element results of a large SSLIM with solid-iron secondary. Various solid iron secondary thicknesses are considered

for SSLIM design to evaluate its effects on the motor performance.

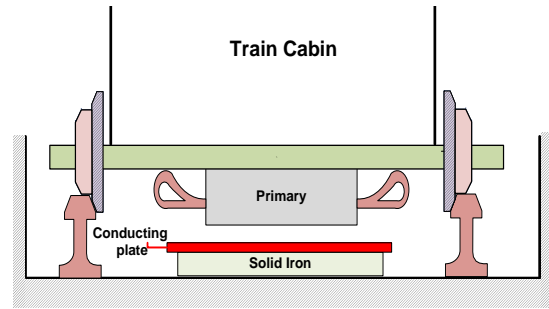


Fig. 2: Rail transportation system with SSLIM

### Sslim Design

In order to evaluate the proposed model, a solid iron SSLIM, that its experimental results are available, is considered. Design parameters of the considered SSLIM is shown in Table 1 [16]. The one\_pole pitch model of the intended motor with solid-iron secondary is shown in Fig. 3.

Table 1: The parameters and dimensions of a single-sided LIM with double layer winding and half-filled end slots [16]

Parameter	Value
Number of phases, $m$	3
Number of pole pair, $p$	3
Pole pitch, $\tau$	0.25 m
Winding pitch, $W_c$	0.194 m
Primary width, $L$	0.101 m
Secondary width, $W$	0.178 m
Mechanical air-gap, $g$	12 mm
Slot width, $w_s$	15 mm
Slot height, $h_s$	30 mm
Primary yoke height, $h_y$	71.6 mm
Secondary height, $h_{ys}$	25.4 mm
Total slots number, $Q_s$	61
Number of slots per pole per phase, $q$	3
Half-filled end slots	14
The conductivity of the secondary, $\sigma_i$	$4.46 \times 10^6$ S/m
Number of turns per phase, $N_s$	108
Rated primary input current, $I$	200 A (rms)

The magnetic saturation in the solid irons as the secondary of SSLIM generates harmonics in magnetic variables, which is not considered in the previously presented analytical methods.

Therefore, consideration of Magnetic field intensities and magnetic flux densities as sinusoidal functions of time is not correct in the solid iron SSLIM performance modeling. In order to consider this effect, the DC B-H

curve of solid iron is modified to an effective B1-H curve [28], in which B1 is the fundamental component of the flux density (Fig. 4). Figs. 5 and 6 show the DC B-H curve and an effective B1-H curve and corresponding relative magnetic permeability for the mild-steel of the secondary [16].

The transverse effect or the third-dimension effect is considered by modifying the secondary conductivity by Russel-Northworthy correction factor [22][30]:

$$\sigma' = k_{\sigma} \cdot \sigma_i \quad (1)$$

$$k_{\sigma} = 1 - \frac{1}{\frac{\pi \cdot L}{\tau} \cdot 2} \cdot \frac{\tanh\left(\frac{\pi \cdot L}{\tau} \cdot \frac{L}{2}\right)}{\left(1 + \tanh\left(\frac{\pi \cdot L}{\tau} \cdot \frac{L}{2}\right) \cdot \tanh\left(\frac{\pi \cdot c}{\tau}\right)\right)} \quad (2)$$

where  $k_{\sigma}$ ,  $\tau$ ,  $\sigma'$  and  $\sigma_{ii}$  are Russel-Northworthy factor, pole pitch, modified and intrinsic secondary conductivity, respectively. Parameters  $c$  and  $L$  are motor design parameters, as shown in Fig. 2.

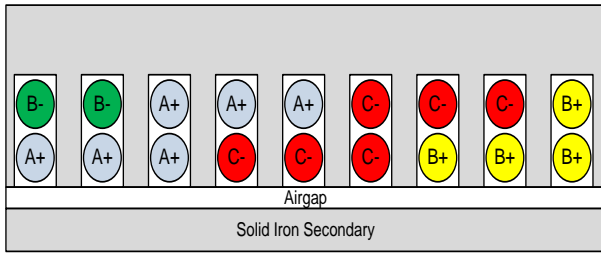


Fig. 3: One-pole pitch model of a SSLIM with a solid-iron secondary.

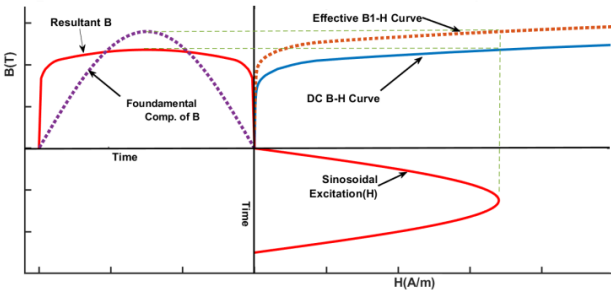


Fig. 4: Modification of the DC B-H curve of solid iron (solid lines) to an effective B1-H curve calculated for the fundamental component of flux density (dashed lines) – considering sinusoidal field intensity.

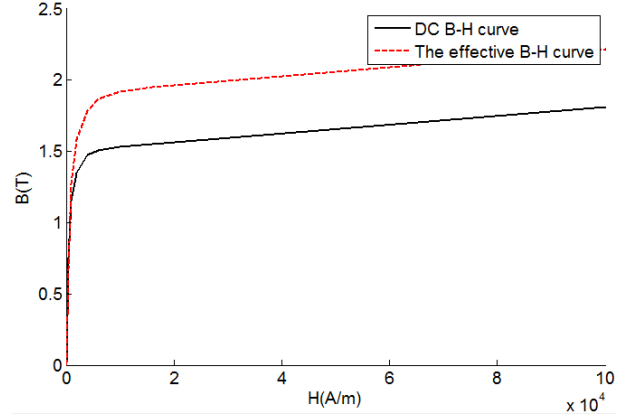


Fig. 5: A comparison between DC and the effective B-H curve for the fundamental component of the flux density - mild steel.

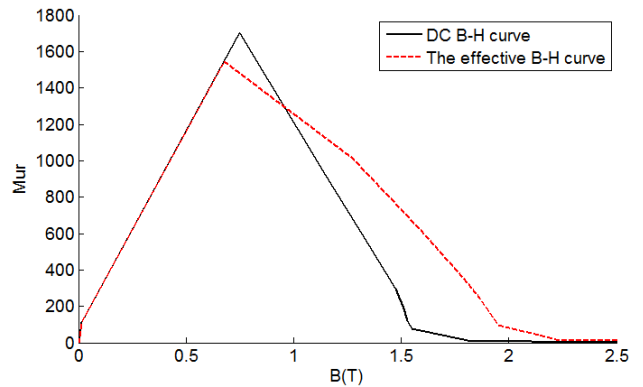


Fig. 6: A comparison between DC and the effective relative magnetic permeability curve for the fundamental component of the flux density - mild steel.

## Finite Element Modeling

In order to predict solid secondary SSLIM performance, FE modeling is employed as a numerical method. The governing differential equations for the 2-D analysis of the proposed structure are:

$$\nabla \times \mathbf{H} = \mathbf{J} \quad (3)$$

$$\nabla \times \mathbf{E} = -\frac{\partial \mathbf{B}}{\partial t} \quad (4)$$

$$\mathbf{B} = \mu \mathbf{H}, \mathbf{J} = \sigma' \cdot \mathbf{E} \quad (5)$$

$$\nabla \cdot \mathbf{B} = 0 \rightarrow \mathbf{B} = \nabla \times \mathbf{A} \quad (6)$$

where,  $H$ ,  $J$ ,  $E$ ,  $B$ ,  $\mu$ ,  $\sigma'$  and  $A$  are magnetic field strength, current density, electric field strength, magnetic flux density, magnetic permeability, modified electrical conductivity and magnetic potential vector, respectively. Then, the resulting differential equation in the solid-iron secondary is:

$$\nabla \times \left( \frac{\nabla \times \mathbf{A}_z}{\mu} \right) = -js\omega \cdot \sigma' \cdot \mathbf{A}_z \quad (7)$$

where  $\omega$ ,  $s$ ,  $\mu$  and  $A_z$  are the supply angular frequency, secondary slip, magnetic permeability and z-axis component of magnetic vector potential, respectively. The end effects are neglected in the simulations due to the low-speed operation of SSLIMs and high electrical-resistivity of solid iron of the secondary. In addition,  $\sigma'$  is employed for solid iron according to (1).

Figures 7 and 8 show magnetic flux distributions of FEM modeling of the designed SSLIM at different frequencies. The flux lines distribution has longer tail and lower penetration depth at 40 Hz than 11 Hz due to the higher induced eddy currents and higher reaction fields of induced eddy currents in the solid iron secondary.

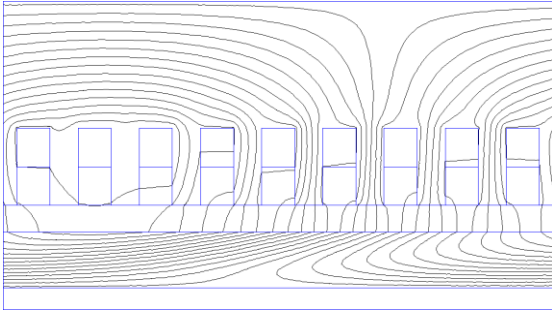


Fig. 7: The magnetic flux distribution in the SSLIM at the  $s = 1$  and the source frequency of 11 Hz with secondary thickness = 25.4 mm

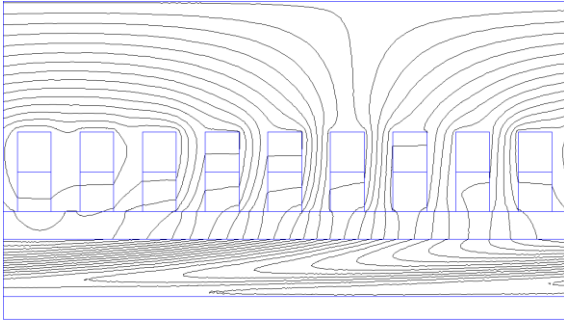


Fig. 8: The magnetic flux distribution in the solid secondary SSLIM at the  $s = 1$  and the source frequency of 40 Hz with secondary thickness = 25.4 mm

### Analytical Modeling

Figure 9 shows the simplified model of a single-sided LIM for analytical calculations. The stator winding is replaced with a current layer, and the magnetic permeability of stator iron is considered infinite. The solid iron of the secondary with finite thickness is replaced with infinite half-space region in perpendicular direction of the secondary iron surface. Given the slotting effect, the air-gap length in Fig. 1 is modified by the Carter factor [22]. The general travelling wave equations are given in (8) to (14) for a solid-iron secondary. It is assumed that the saturation is only in the x direction and the solid iron has a linear magnetic

characteristic in the y direction. The function  $B=a \cdot H^b$  is considered for the B-H curve with constants a and b. The mathematical assumptions for magnetic field strength and magnetic permeability of solid iron are given by (15) to (17). Then, the solutions for the magnetic fields in the solid-iron (region 2) are presented by (18) to (20) for half space and infinite secondary thickness. Besides, their unknown parameters are then calculated using (21) to (26). The field solutions for air-gap (region 1) are given in (27) to (31). The C1 and C'1 constants in (30) and (31) are then respectively calculated using the boundary conditions in (33) to (35) and presented in (40) and (41).

$$\frac{\partial H_{y,2}}{\partial x} - \frac{\partial H_{x,2}}{\partial y} = \sigma' \cdot E_{z,2} \quad (8)$$

$$\frac{\partial B_{x,2}}{\partial x} + \frac{\partial B_{y,2}}{\partial y} = 0 \quad (9)$$

$$\frac{\partial E_{z,2}}{\partial y} = -\frac{\partial B_{x,2}}{\partial t} \quad (10)$$

$$\frac{\partial E_{z,2}}{\partial x} = \frac{\partial B_{y,2}}{\partial t} \quad (11)$$

$$B_{y,2} = \mu_y \cdot H_{y,2} \quad (12)$$

$$B_{x,2} = a \cdot H_{x,2}^b \quad (13)$$

$$\frac{\partial}{\partial x} = -j \frac{\pi}{\tau} \quad (14)$$

$$\frac{\partial^2 H_{x,2}}{\partial y^2} - \left( j s \omega \cdot \sigma' + \frac{1}{\mu_y} \cdot \left( \frac{\pi}{\tau} \right)^2 \right) \cdot B_{x,2} = 0 \quad (15)$$

$$\mu_x = \frac{\mu_{x,0}}{\left( 1 + \frac{y}{y_0} \right)^2} \quad (16)$$

$$y \leq 0, \left( \mu_{x,0} = \frac{B_0}{H_0} = a \cdot H_0^{b-1} \right) \quad (17)$$

$$H_{x,2} = \left( 1 + \frac{y}{y_0} \right)^\alpha \cdot H_0 \cdot e^{j(\omega t - \frac{\pi}{\tau} \cdot x)} \quad (18)$$

$$B_{x,2} = \left( 1 + \frac{y}{y_0} \right)^{\alpha-2} \cdot B_0 \cdot e^{j(\omega t - \frac{\pi}{\tau} \cdot x)} \quad (19)$$

$$B_{y,2} = \frac{y_0}{\alpha-1} \cdot j \cdot \frac{\pi}{\tau} \cdot \left( 1 + \frac{y}{y_0} \right)^{\alpha-1} \cdot B_0 \cdot e^{j(\omega t - \frac{\pi}{\tau} \cdot x)} \quad (20)$$

where  $\mu_x$ ,  $\mu_y$ ,  $B_x$ ,  $B_y$ ,  $H_x$ ,  $H_y$ ,  $\tau$ ,  $y_0$ ,  $B_0$  and  $H_0$  are x and y component of magnetic permeability, magnetic flux density, magnetic field intensity, pole pitch, penetration depth, magnetic flux density at the surface of solid iron

and magnetic field strength at the surface of solid iron, respectively.  $\alpha$  is described in (21) and the constant  $b$  can be considered zero for simplicity since it will not affect the accuracy of analysis [30][31].

$$\alpha \cdot (\alpha - 1) \cdot \frac{1}{y_0^2} \cdot \underline{H}_{x,2} = \left( js\omega \cdot \sigma' \cdot \mu_{x,0} + \frac{\mu_{x,0}}{\mu_y} \cdot \left( \frac{\pi}{\tau} \right)^2 \right) \underline{H}_{x,2} \quad (21)$$

$$\alpha = \alpha' + j \cdot \alpha'' \quad (22)$$

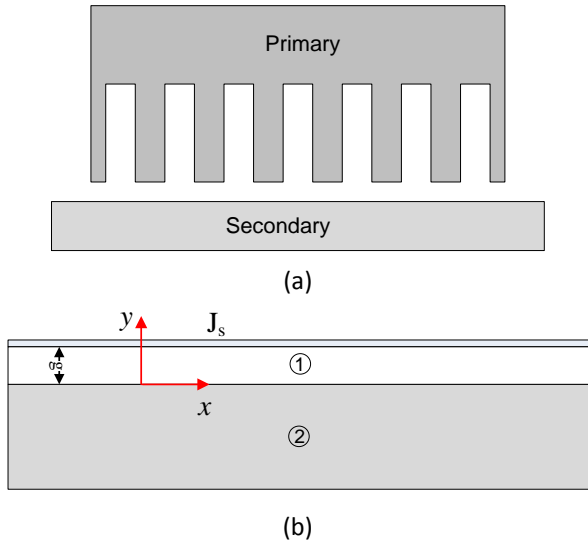


Fig. 9: (a) The schematic model of a single-sided LIM with a solid-iron secondary, (b) The simplified model for analytical calculations.

$$\alpha' = \frac{2}{1-b} \quad (23)$$

$$\alpha'' = \frac{-F + \sqrt{F^2 + 4\alpha' \cdot (\alpha' - 1)}}{2} \quad (24)$$

$$F = \frac{(2\alpha' - 1) \cdot \left( \frac{\pi}{\tau} \right)^2}{\mu_y \cdot s \cdot \omega \cdot \sigma'} \quad (25)$$

$$y_0 = \sqrt{\frac{(2\alpha' - 1) \cdot \alpha''}{\mu_{x,0} \cdot s \cdot \omega \cdot \sigma'}} \quad (26)$$

$$\frac{\partial^2 \underline{B}_{x,1}}{\partial x^2} + \frac{\partial^2 \underline{B}_{x,1}}{\partial y^2} = 0 \quad (27)$$

$$\frac{\partial^2 \underline{B}_{y,1}}{\partial x^2} + \frac{\partial^2 \underline{B}_{y,1}}{\partial y^2} = 0 \quad (28)$$

$$\frac{\partial \underline{B}_{x,1}}{\partial x} + \frac{\partial \underline{B}_{y,1}}{\partial y} = 0 \quad (29)$$

$$\underline{B}_{x,1}(y) = (C_1 \cdot \cosh\left(\frac{\pi}{\tau} \cdot y\right) + C_1' \cdot \sinh\left(\frac{\pi}{\tau} \cdot y\right)) e^{j(\omega t - \frac{\pi}{\tau} \cdot x)} \quad (30)$$

$$\underline{H}_{x,1}(y) = \frac{(C_1 \cdot \cosh\left(\frac{\pi}{\tau} \cdot y\right) + C_1' \cdot \sinh\left(\frac{\pi}{\tau} \cdot y\right))}{\mu_0} e^{j(\omega t - \frac{\pi}{\tau} \cdot x)} \quad (31)$$

$$\underline{B}_{y,1}(y) = j(C_1 \cdot \sinh\left(\frac{\pi}{\tau} \cdot y\right) + C_1' \cdot \cosh\left(\frac{\pi}{\tau} \cdot y\right)) e^{j(\omega t - \frac{\pi}{\tau} \cdot x)} \quad (32)$$

$$\underline{H}_{x,1}(y=0) = \underline{H}_{x,2}(y=0) \quad (33)$$

$$\underline{B}_{y,1}(y=0) = \underline{B}_{y,2}(y=0) \quad (34)$$

$$\underline{H}_{x,1}(y=g) = \underline{J}_s \quad (35)$$

$$\underline{J}_s = J_m \cdot e^{j(\omega t - \frac{\pi}{\tau} \cdot x - \phi)} \quad (36)$$

$$J_m = \frac{2 \cdot m \cdot k_W \cdot N_s}{2 \cdot p \cdot \tau} \cdot \sqrt{2} \cdot I \quad (37)$$

$$k_W = \frac{\sin\left(\frac{\pi}{6}\right)}{q \cdot \sin\left(\frac{\pi}{6 \cdot q}\right)} \cdot \sin\left(\frac{W_c}{\tau} \cdot \frac{\pi}{2}\right) \quad (38)$$

$$C_1 \cdot \cosh\left(\frac{\pi}{\tau} \cdot g\right) + C_1' \cdot \sinh\left(\frac{\pi}{\tau} \cdot g\right) = \mu_0 \cdot J_m \cdot e^{-j\phi} \quad (39)$$

$$C_1 = \mu_0 \cdot H_0 \quad (40)$$

$$C_1' = \frac{y_0}{\alpha - 1} \cdot \frac{\pi}{\tau} \cdot B_0 \quad (41)$$

where,  $\mu_0$ ,  $k_W$ ,  $J_s$  and  $J_m$  are the magnetic permeability of vacuum, armature winding factor, current layer linear current density and its amplitude, respectively.

The parameter  $H_0$  is obtained using (42) where the under-relaxation coefficient of 0.9 is used for iteration process of  $H_0$  calculation, which causes faster convergence [13]:

$$H_0 = \left| \frac{J_m}{\cosh\left(\frac{\pi}{\tau} \cdot g\right) + \frac{y_0 \cdot \pi \cdot \mu_{x,0}}{(\alpha - 1) \cdot \tau \cdot \mu_0} \cdot \sinh\left(\frac{\pi}{\tau} \cdot g\right)} \right| \quad (42)$$

$$\mu_{x,0} = 0.9 \cdot \mu_{x,0} \cdot (\text{old}) + 0.1 \cdot \mu_{x,0} \cdot (\text{new}) \quad (43)$$

$$H_0 = 0.9 \cdot H_0 \cdot (\text{old}) + 0.1 \cdot H_0 \cdot (\text{new}) \quad (44)$$

## Results and Discussion

### A. FEM simulation results

The comparison between the finite element results of the current work and the experimental results of [16] for

thrust forces are shown in Fig. 11. The correction factor for solid iron electrical conductivity is calculated by using (1) is 0.29.

It is shown that the results of the calculated thrust forces using FEM coincide well with experimental results.

The solid iron secondary thickness is increased from 25.4 mm to 100 mm to evaluate secondary thickness effect on thrust force (Figs. 11 and 12).

The thrust forces increase with 100 mm secondary thickness in low rotor frequencies range (higher speeds), where penetration depth is higher than secondary thickness (Fig. 13).

The magnetic flux distributions in the single-sided LIM at slip 1 and the source frequencies of 11 Hz, and 40 Hz are respectively shown in Figs. 10, and 11 with 100 mm secondary thickness.

*B. Analytical simulation results*

The thrust force is analytically calculated using the Maxwell’s stress tensor at secondary surface by (45):

$$F = L' \cdot \text{Re} \left( \int H_x \cdot B_y^* dx \right) = \frac{L' \cdot p \cdot y_o \cdot \alpha''}{(\alpha' - 1)^2 + \alpha''^2} \cdot B_o \cdot H_o$$

$$L' = L + g \dots 2g \tag{45}$$

where,  $L'$ , is effective transverse length for thrust force analysis [17].

Figure 14 shows a comparison between the analytical calculations of the thrust forces for infinite half space assumption for secondary and FEM results, which demonstrate good correspondence with results of 100 mm secondary thickness for all speeds.

The analytical results even coincide well with FEM results for 25.4 mm secondary thickness at low speeds for 40 Hz because penetration depth is smaller than secondary thickness.

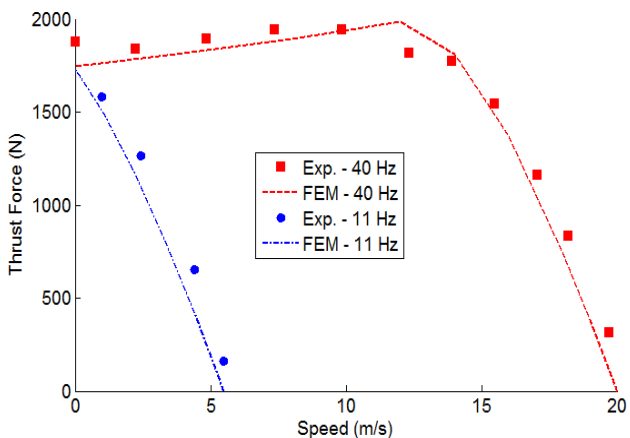


Fig. 10: A comparison between the thrust forces by the finite element proposed analysis and the experimental results [16].

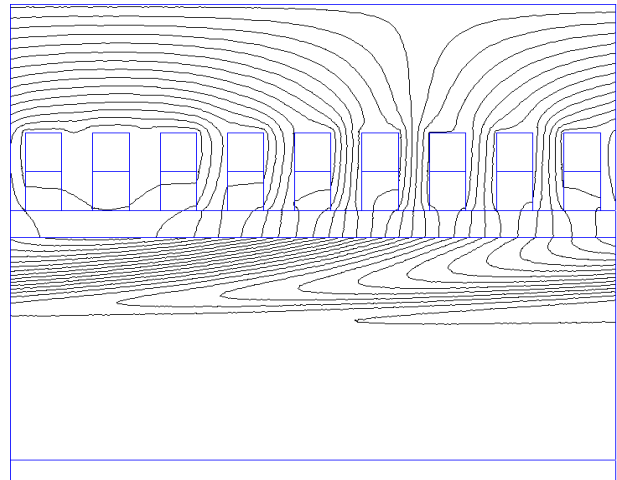


Fig. 11: The magnetic flux distribution in the single-sided linear induction motor at the slip  $s = 1$  and the source frequency of 11 Hz with secondary thickness = 100 mm.

To take into account the secondary thickness effect on analytical calculations, the parameter,  $\alpha''$  is recalculated by:

$$\alpha'' = \frac{y_o^2 \cdot s \omega \cdot \sigma' \cdot \mu_{x,0}}{(2\alpha' - 1)} \tag{46}$$

$$y_o = 1.1 \dots 1.2 \cdot h_{ys} \tag{47}$$

In (47), penetration depth ( $y_o$ ) is considered equal to 1.1 to 1.2 times of secondary thickness,  $h_{ys}$  to take into account leakage flux to outside of secondary region. The calculated thrust force using (45) shows well coincidence with experimental and FEM results at all speed and frequency ranges (Fig. 15).

The end effects are not considered in the FEM and the analytical calculations due to the negligible impacts on thrust forces of single-sided LIMs with solid-iron secondary.

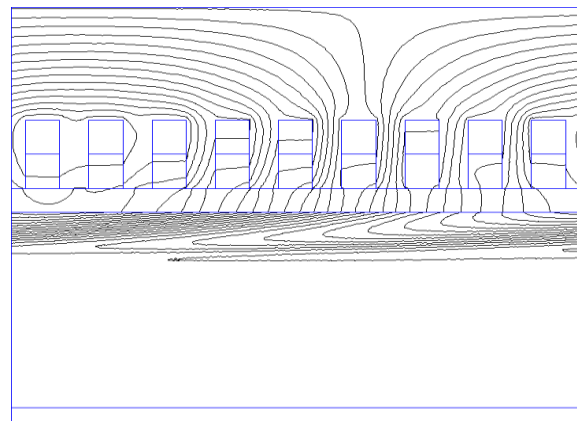


Fig. 12: The magnetic flux distribution in the single-sided linear induction motor at the slip  $s = 1$  and the source frequency of 40 Hz with secondary thickness of 100 mm.

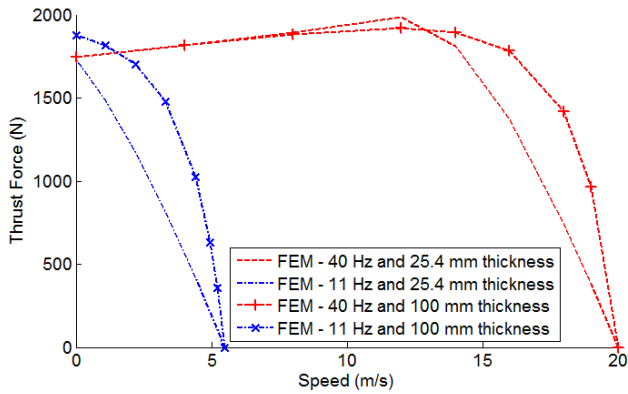


Fig. 13: A comparison between the thrust forces by the finite element analysis with different secondary thicknesses.

C. Discussion

The y-component of the magnetic permeability of solid iron  $\mu_y$ , is assumed equal to  $\mu_{x,0}$  in (21) and (25) because the x-component of the magnetic field is stronger than the y-component of the magnetic field in the secondary solid iron.

The given electrical conductivity of solid iron are all at 20 oC and the thrust forces of linear induction motors could be different at higher temperatures. Figs. 13 and 14 show influential effect of secondary thickness on the produced thrust force. For example, at slip equal 0.125 for 40 Hz, the thrust force almost becomes double for 100 mm secondary thickness in comparison with 25.4 mm secondary thickness. Using (26), penetration depth,  $y_0$  at slip equal 0.125 is calculated equal to 42 mm. Increasing secondary thickness could improves performance of SSLIM with solid iron secondary. The secondary thickness is decreased to half, 12.7 mm to evaluate smaller secondary thickness on LIM performance (Figs. 16 and 17). The thrust forces decrease drastically and the analytical method predicts thrust force with acceptable accuracy (Fig. 18).

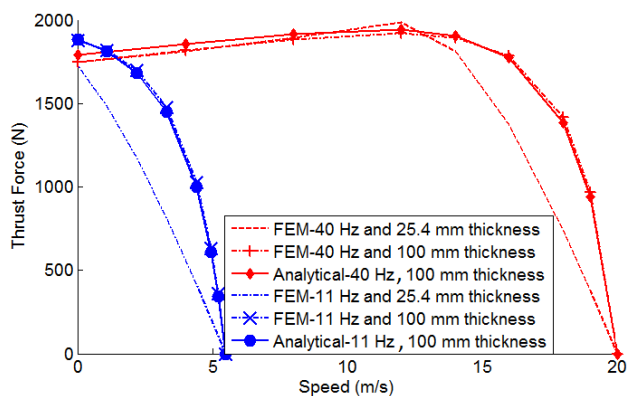


Fig. 14: A comparison between the thrust forces by the analytical analysis and FEM results.

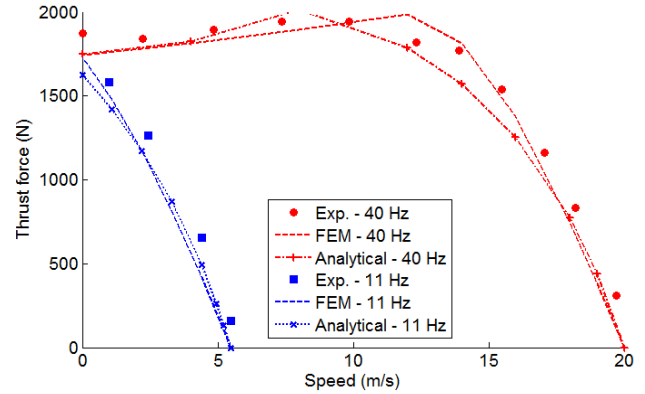


Fig. 15: A comparison between the thrust forces by the analytical analysis, FEM results and the experimental results [16] considering secondary thickness of 25.4 mm.

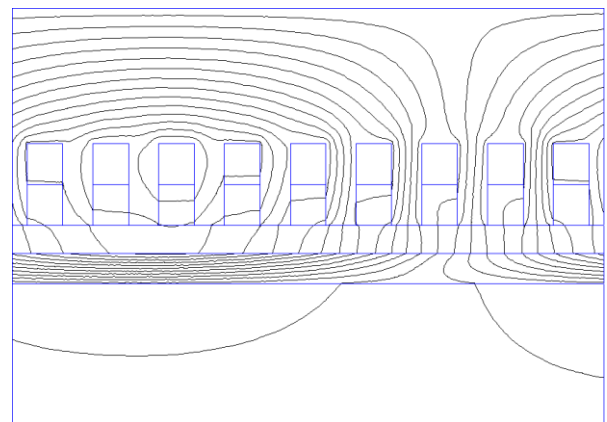


Fig. 16: The magnetic flux distribution in the single-sided linear induction motor at the slip  $s = 1$  and the source frequency of 11 Hz with secondary thickness of 12.7 mm.

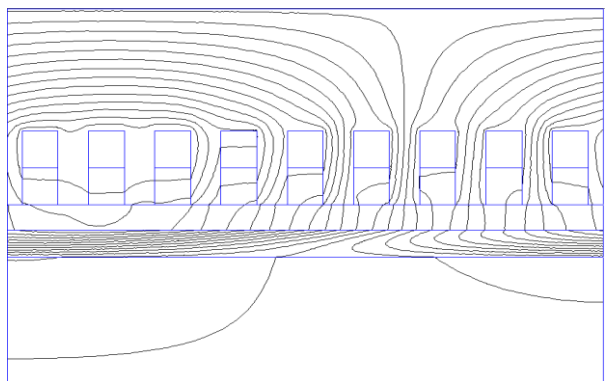


Fig. 17: The magnetic flux distribution in the single-sided linear induction motor at the slip  $s = 1$  and the source frequency of 40 Hz with secondary thickness of 12.7 mm.

Conclusion

SSLIM is one of the candidates for propulsion part of this system. In this paper, a 2D FEM analysis of a solid iron secondary SSLIM is presented based on time harmonic method with taking into account effective B-H

curve. In addition, a new 2D analytical method of the proposed SSLIM is presented considering solid iron saturation and the skin effects for eddy current analysis.

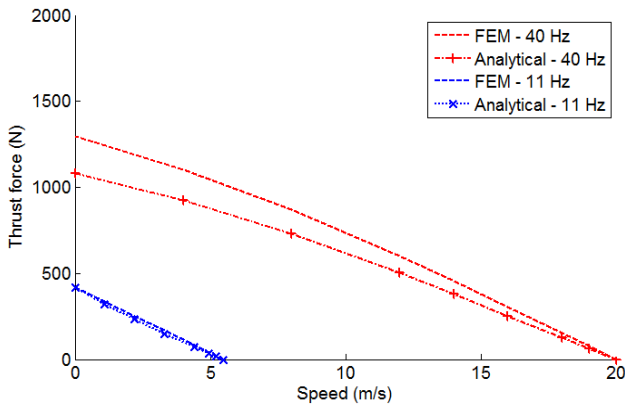


Fig. 18: A comparison between the thrust forces by the analytical analysis, FEM results and the experimental results considering secondary thickness = 12.7 mm

The analytical method could be used for traveling wave eddy currents and with consideration of air-gaps like in induction machines. The presented analytical method is simple and fast, and it could also be used for loss analysis in solid irons and steels for solid rotor synchronous machines with finite thickness. The simulation results of the proposed methods show acceptable accuracy with experimental ones. Due to acceptable accuracy and fast response of the presented analytical method, it could be employed as an effective tool in design and optimization of large solid iron secondary SSLIM employed in transportation systems. The presented analytical method could be used to calculate eddy currents losses in the solid iron rotor of asynchronous machines as well.

### Author Contributions

S. E. Abdollahi and M. Mirzayee designed the experiments, collected the data and carried out the data analysis. They also interpreted the results and wrote the manuscript.

### Acknowledgment

The authors would like to thank the anonymous reviewers for their comments which lead to improving the quality of the paper.

### Conflict of Interest

The authors declare that there is no conflict of interests regarding the publication of this manuscript.

### Abbreviations

$g$	Mechanical air-gap
$h_s$	Slot height
$h_y$	Primary yoke height
$h_{ys}$	Secondary height

$I$	Rated primary input current
$L$	Primary width
LIM	Linear induction motor
$m$	Number of phases
$N_s$	Number of turns per phase
$p$	Number of pole pair
$q$	Number of slots per pole per phase
$Q_s$	Total slots number
$\sigma_i$	Conductivity of the secondary
SSLIM	Single Sided LIM
$\tau$	Pole pitch
$W$	Secondary width
$W_c$	Winding pitch
$w_s$	Slot width
$y_0$	Penetration depth

### References

- [1] R. Hellinger, P. Mních, "Linear motor-powered transportation: history, present status, and future outlook," *Proceedings of the IEEE*, 97(9): 1892-1900, 2009.
- [2] S. Aleksandrov, T. Overboom, E. Lomonova, "Design optimization and performance comparison of two linear motor topologies with PM-Less tracks," *IEEE Transactions on Magnetics*, 54(11): 1-8, 2018.
- [3] I. Boldea, M. Pucci, W. Xu, "Design and control for linear machines, drives, and MAGLEVs—Part I," *IEEE Transactions on Industrial Electronics*, 65(1): 7423-7426, 2018.
- [4] S. E. Abdollahi, M. Mirzayee, M. Mirsalim, "Design and analysis of a double-sided linear induction motor for transportation," *IEEE Transactions on Magnetics*, 51(7): 1-7, 2015.
- [5] S. E. Abdollahi, S. Vaez-Zadeh, "Back EMF analysis of a novel linear flux switching motor with segmented secondary," *IEEE Transactions on Magnetics*, 50(4): 1-9, 2014.
- [6] J. Wang, Z. Lin, D. Howe, "Analysis of a short-stroke, single-phase, quasi-Halbach magnetised tubular permanent magnet motor for linear compressor applications," *IET Electric Power Applications*, 2(3): 193-200, 2008.
- [7] B. Kou, J. Luo, X. Yang, L. Zhang, "Modeling and analysis of a novel transverse-flux flux-reversal linear motor for long-stroke application," *IEEE Transactions on Industrial Electronics*, 63(10): 6238-6248, 2016.
- [8] D. K. Hong, D. Joo, J. W. Kim, B. C. Woo, D. H. Koo, "Development of thrust force 6 kN class transverse flux linear motor with synchronous control for direct drive applications," *International Journal of Precision Engineering and Manufacturing*, 16(1): 191-196, 2015.
- [9] R. Cao, Y. Jin, M. Lu, Z. Zhang, "Quantitative comparison of linear flux-switching permanent magnet motor with linear induction motor for electromagnetic launch system," *IEEE Transactions on Industrial Electronics*, 65(9): 7569-7578, 2018.
- [10] A. Musolino, M. Raugi, R. Rizzo, M. Tucci, "Optimal design of EMALS based on a double-sided tubular linear induction motor," *IEEE Transactions on Plasma Science*, 43(5): 1326-1331, 2015.
- [11] H. W. Lee, K. C. Kim, J. Lee, "Review of maglev train technologies," *IEEE transactions on magnetics*, 42(7): 1917-1925, 2006.
- [12] S. Nasar, L. Del Cid, "Propulsion and levitation forces in a single-sided linear induction motor for high-speed ground transportation," *Proceedings of the IEEE*, 61(5): 638-644, 1973.
- [13] A. Shiri, A. Shoulaie, "Design optimization and analysis of single-sided linear induction motor, considering all phenomena," *IEEE Transactions on energy conversion*, 27(2): 516-525, 2012.

- [14] M. Flankl, L. de Oliveira Baumann, A. Tüysüz, J. W. Kolar, "Energy Harvesting With Single-Sided Linear Induction Machines Featuring Secondary Conductive Coating," *IEEE Transactions on Industrial Electronics*, 66(6): 4880-4890, 2019.
- [15] S. Nonaka, T. Higuchi, "Elements of linear induction motor design for urban transit," *IEEE Transactions on Magnetics*, 23(5): 3002-3004, 1987.
- [16] J. Gieras, A. Eastham, G. Dawson, "Performance calculation for single-sided linear induction motors with a solid steel reaction plate under constant current excitation," *IEE Proceedings B - Electric Power Applications*, 132(4): 185-194, 1985.
- [17] J. J. Stickler, "A study of single-sided linear induction motor performance with solid iron secondaries," *IEEE Transactions on Vehicular Technology*, 31(2): 107-112, 1982.
- [18] M. Mirsalim, A. Doroudi, J. Moghani, "Obtaining the operating characteristics of linear induction motors: A new approach," *IEEE Transactions on magnetics*, 38(2): 1365-1370, 2002.
- [19] J. H. Lee, H. Y. Kim, M. J. Jun, S. C. Lee, "Optimum shape design of single-sided linear induction motors using response surface methodology and finite element method," in *Proc. International Conference on Electrical Machines and Systems (ICEMS)*: 1-5, 2011.
- [20] G. Lv, D. Zeng, T. Zhou, Z. Liu, "Investigation of forces and secondary losses in linear induction motor with the solid and secondary losses in linear induction motor with the solid and laminated back iron secondary for metro," *IEEE Transactions on Industrial Electronics*, 64(6): 4382-4390, 2017.
- [21] G. Lv, T. Zhou, D. Zeng, "Influence of the ladder-slit secondary on reducing the edge effect and transverse forces in the linear induction motor," *IEEE Transactions on Industrial Electronics*, 65(9): 7516-7525, 2018.
- [22] J. F. Gieras, *Linear Induction Drives*: Clarendon, 1994.
- [23] P. D. Agarwal, "Eddy-current losses in solid and laminated iron," *Transactions of the American institute of electrical engineers, Part I: Communication and Electronics*, 78(2): 169-181, 1959.
- [24] I. Boldea, M. Babescu, "Multilayer approach to the analysis of single-sided linear induction motors," *Proceeding of the Institution of Electrical Engineers*, 125(4): 283-287, 1978.
- [25] L. R. Neuman (1948), *Skin effect in ferromagnetic bodies*, Gostekhizdat, M. (in Russian).
- [26] K. Pillai, "Fundamental-frequency eddy-current loss due to rotating magnetic field. Part 1: Eddy-current loss in solid rotors," *Proceedings of the Institution of Electrical Engineers*, 119(3): 407-410, 1969.
- [27] J. Gieras, "Analytical method of calculating the electromagnetic field and power losses in ferromagnetic halfspace, taking into account saturation and hysteresis," *Proceedings of the Institution of Electrical Engineers*, 124(11): 1098-1104, 1977.
- [28] S. Nasar, G. Xiong, Z. Fu, "Eddy-current losses in a tubular linear induction motor," *IEEE transactions on magnetics*, 30, no. 4): 1437-1445, 1994.
- [29] G. Lv, D. Zeng, T. Zhou, "Analysis of Secondary Losses and Efficiency in Linear Induction Motors with Composite Secondary Based on Space Harmonic Method," *IEEE Transactions on Energy Conversion*, 32(4): 1583-1591, 2017.
- [30] M. Jagiela, T. Garbiec, "Evaluation of rotor-end factors in solid-rotor induction motors," *IEEE Transactions on Magnetics*, 48(1): 137-142, 2012.
- [31] N. Kesavamurthy P. Rajagopalan, "The polyphase induction machine with solid iron rotor," *Transactions of the American Institute of Electrical Engineers. Part III: Power Apparatus and Systems*, 78(4): 1092-1097, 1959.

## Biographies



**Seyed Ehsan Abdollahi** was born in Sari, Iran. He received the B.Sc. degree from the Amirkabir University of Technology, Tehran, Iran, in 2002, the M.Sc. degree from Iran University of Science and Technology, Tehran, Iran, in 2005, and the Ph.D. degree from University of Tehran, Tehran, Iran, in 2014, all in Electric Power Engineering. He joined the Babol Noshirvani University of Technology, Babol, Iran, as an Assistant Professor. His current research interests include electric machine design and modeling, electric vehicle and power electronics.

**Mehran Mirzaee** received the B.Sc. and M.Sc. degrees from Amirkabir University of Technology, Tehran, Iran. He was a Research Assistant with the Electrical Machines and Transformer Research Laboratory, Department of Electrical Engineering, Amirkabir University of Technology.

### Copyrights

©2020 The author(s). This is an open access article distributed under the terms of the Creative Commons Attribution (CC BY 4.0), which permits unrestricted use, distribution, and reproduction in any medium, as long as the original authors and source are cited. No permission is required from the authors or the publishers.



### How to cite this paper:

S. E. Abdollahi, M. Mirzaei, "Analysis of a linear induction motor with solid iron secondary," *Journal of Electrical and Computer Engineering Innovations*, 6(1): 77-85, 2018.

**DOI:** 10.22061/JECEI.2019.1079

**URL:** [http://jecei.sru.ac.ir/article\\_1079.html](http://jecei.sru.ac.ir/article_1079.html)

